
Article:
Mawson, Eleanor E., Lee, Katherine C. and Hill, Jon orcid.org/0000-0003-1340-4373 (2022) Sea level rise and the Great Barrier Reef the future implications on reef tidal dynamics. Journal of Geophysical Research: Oceans. e2021JC017823. ISSN 2169-9291

https://doi.org/10.1029/2021JC017823

JGR Oceans

RESEARCH ARTICLE
10.1029/2021JC017823

Sea Level Rise and the Great Barrier Reef: The Future Implications on Reef Tidal Dynamics

Eleanor E. Mawson[1], Katherine C. Lee[1], and Jon Hill[1]

[1]Department of Environment and Geography, University of York, York, UK

Key Points:

- Sea-level rise alters the tidal dynamics in the Great Barrier Reef
- Changes in tidal dynamics is spatially complex, with changes in tidal range of up to 10% of the sea-level rise
- The two main tidal component amplitudes change in the opposite direction

Supporting Information:

Supporting Information may be found in the online version of this article.

Correspondence to:

E. E. Mawson and J. Hill,
em2029@hw.ac.uk;
jon.hill@york.ac.uk

Citation:

Mawson, E. E., Lee, K. C., & Hill, J. (2022). Sea level rise and the Great Barrier Reef: The future implications on reef tidal dynamics. *Journal of Geophysical Research: Oceans*, *127*, e2021JC017823. https://doi.org/10.1029/2021JC017823

Received 4 AUG 2021
Accepted 3 JUL 2022

Author Contributions:

Conceptualization: Eleanor E. Mawson, Jon Hill
Formal analysis: Eleanor E. Mawson
Methodology: Eleanor E. Mawson, Jon Hill
Software: Eleanor E. Mawson
Supervision: Jon Hill
Validation: Eleanor E. Mawson, Katherine C. Lee, Jon Hill
Visualization: Eleanor E. Mawson, Jon Hill
Writing – original draft: Eleanor E. Mawson
Writing – review & editing: Eleanor E. Mawson, Katherine C. Lee, Jon Hill

Abstract Predicted sea-level rise (SLR) is anticipated to alter tidal dynamics in the future and this will in turn alter coastal ecosystems, flood risk, and geomorphology. Coral reefs are bathymetrically complex environments where tides play a crucial role in larval and nutrient dispersal. This complexity makes coral reef environments challenging to simulate numerically as a large area needs to be simulated but also with high resolution to capture the complexity. To investigate the influence of SLR on tidal dynamics in coral reef systems we use an unstructured mesh numerical model, with spatially varying resolution, of the Great Barrier Reef (GBR). The present-day conditions and a total of three future SLR scenarios are considered based on the RCP scenarios. The results focus on the major tidal constituents and tidal range. The M_2 constituent generally decreases across gauge locations as sea-level rises but S_2 generally increases. O_1 and K_1 display small variations or no change. The tidal range experiences ±10% variation depending on the gauge location, meaning it is spatially varying and alters SLR by up to 10%. Overall, SLR will influence tidal dynamics across the GBR altering coastal flooding risk with a spatially varying impact. Management schemes should consider tidal range changes in addition to increases in extreme weather conditions to provide adequate preservation of the coastline, coastal cities and infrastructure in the future. Moreover, changes in tidal patterns and dynamics may alter the distributions of reef spores and larvae and should be included in future plans of reef management.

Plain Language Summary Sea-level rise (SLR) alters the ebb and flow of tidal currents, as well as altering the tidal range. As sea level is projected to rise in the future it is anticipated that coastal regions will experience a change in tidal patterns also. In turn this will affect coastal flood risk, ecosystems and geomorphology. Coral reefs are complex environments with rapidly changing bathymetry but tides can play a vital role in their functioning. To determine the influence of SLR on changing tidal features in such complex environments, we simulate tides on the Great Barrier Reef, the world's largest reef ecosystem. In order to determine the effects of SLR, spatially-varying resolution, where model resolution varies across the simulation area, can be used to capture the bathymetric complexity whilst simulating a large enough region. We carry out simulations consisting of the present-day and three SLR scenarios. Results show complex spatial changes in tidal dynamics with some areas displaying little change, but others displaying a decrease or increase in tidal range that is around 10% of the sea level rise. Coastal management plans should take into consideration both SLR and tidal range changes to protect coastal cities and infrastructure in the future.

1. Introduction

Throughout the 20th century, the global mean sea level (GMSL) grew rapidly with an average rate of 1.4–1.7 mm/yr (Church & White, 2006; Kopp et al., 2016). The rate accelerated in the latter half of the 20th century and into the 21st century (Dangendorf et al., 2019) with the sea-level rise (SLR) estimated to be 3.2 mm/yr between 1993 and 2010 (Dangendorf et al., 2017), which is the fastest rise in the past 3000 years (Kopp et al., 2016). These changes in global sea level are not spatially homogeneous, with large variations in rates across the globe (Bromirski et al., 2011). Factors that influence spatial variability of SLR include ice sheet and glacier melt (Bessell-Browne et al., 2017; Dangendorf et al., 2017), ocean thermal expansion (Bessell-Browne et al., 2017), inland water storage (Church et al., 2006; Dangendorf et al., 2017) and geodynamic processes (Church et al., 2016; Idier et al., 2019). These changes in sea level also then affect the tidal dynamics, particularly in shallow, coastal regions (e.g., Green, 2010; Harker et al., 2019; Pelling & Green, 2014; Pickering et al., 2012, 2017).

Fundamentally, tides are governed by three main criteria: coastal and ocean basin position and morphology which affects regional tidal flow; plate tectonic placement which governs shelf width and coastal embayment morphology; and sea level which is linked to the previous criteria (Collins et al., 2018). Previous studies have examined

the changes of tidal dynamics with respect to sea level change using either historical records (e.g., Gehrels et al., 1995; Greenberg et al., 2012) or numerical models (e.g., Green, 2010; Harker et al., 2019; Pelling & Green, 2014; Pickering et al., 2012, 2017). Previous modeling studies have focused on global tides or continental shelves. Pickering et al. (2017) conducted a global study including observations from shelf seas. They concluded that the four tidal constituents (K_1, O_1, M_2 and S_2) increased or decreased depending on the region. Changes in the semidiurnal constituents (M_2 and S_2) are more likely to occur in shelf seas such as the GBR, whereas changes in diurnal constituents (K_1 and O_1) are limited to Asian Seas. Thirteen coastal cities including Chittagong, Ningbo, and Rangoon display ±10% mean high water (MHW) which is equal to 1 m SLR at 136 coastal cities, where some of the worlds largest tidal ranges are found (Pickering et al., 2017). Furthermore, Green (2010) conducted a global study with observed increases in the M_2 amplitude but small deviations in the K_1 amplitude. Both of these global studies observed variations in the M_2 amplitude across the European Shelf and the Bay of Fundy, North Atlantic. In large reef complexes, such as the GBR, there was little change in this global-scale of modeling (Green, 2010). Historically, M_2 amplitude displays an increase with SLR in the Bay of Fundy (Gehrels et al., 1995; Greenberg et al., 2012), but variations of −10% or +10% across the European Shelf which related to observed reductions in bed friction dampening, changes in resonance properties and increased reflection of the coast (Idier et al., 2019). Coastal defences may influence the SLR on the European Shelf because tides appear sensitive to <1 m rise in areas with defences (Pelling et al., 2013; Pelling & Green, 2014).

Tides also play a vital role in coral reef environments, which are sensitive to SLR (Ludington, 1979; Wolanski & Spagnol, 2000) and form part of the ecosystem services, including flood defences in those regions (Beck et al., 2018). Since 1990, observed sea levels have increased on the Great Barrier Reef (GBR) by 1–2 mm/yr and in accordance with mid-to-high emission scenarios, sea levels could rise between 0.3 and 0.9 m by 2100 on the central GBR (Morrison & Hughes, 2016). The Intergovernmental Panel on Climate Change (IPCC) scenarios predict that for RCP8.5 rates could be as high as approximately 12 mm/yr, whilst RCP 6.0 and RCP4.5 show rates of change between 6 and 8 mm/yr and RCP 2.6 significantly lower at 4 mm/yr (Pörtner et al., 2019). Overall, predicted SLR appears to be similar to global mean sea-level (GMSL) rise across most of Australia's coastline (Al-Nasrawi et al., 2018; Church et al., 2016; McInnes et al., 2015; Zhang et al., 2017). Reefs are sensitive to various parameters such as water depth, light intensity, ocean temperature, ocean chemistry and extreme weather events including storm-surges (Hoegh-Guldberg et al., 2017; Morrison & Hughes, 2016). Reefs have experienced a 50% decline throughout the tropical regions globally between the last 30–50 years (Hoegh-Guldberg et al., 2017). With changes in ocean circulation governed by SLR, they may decline further (Ludington, 1979; Wolanski & Spagnol, 2000). Changes will cause systemic alterations such as increases in erosion from storms; waves and currents; increases in sedimentology from human settlements; disturbances in larval spawning and settlement; changes in geomorphology and reduction of water quality on the reef which causes a chain reaction of further impacts (Burgess et al., 2007; Chazottes et al., 2017; Church & White, 2006). Changes in ocean circulation will affect currents encountering islands or reefs (Vouriot et al., 2019), the re-circulation of the water allows eddies to form in the lee. These are hundreds of kilometres in size and last for several weeks (Burgess et al., 2007). Sea-level rise enhances these currents and larvae, and marine life can become immersed in the eddies and cannot escape them, this reduces their dispersal and connectivity with other populations further afield (Burgess et al., 2007; Wolanski & Spagnol, 2000).

This heterogeneous flow on coral reefs is due to reefs developing a complex bathymetry and topography making tidal modeling difficult (Harker et al., 2019; Seifi et al., 2019) as both high resolution and a large area need to be simulated (Burgess et al., 2007; Delandmeter et al., 2017; Storlazzi et al., 2011). To simulate tides in coral reef environments, unstructured mesh models are the best solution as they can fulfill the need for high resolution where needed (Lambrechts, Hanert, et al., 2008; Seifi et al., 2019; Storlazzi et al., 2011). The use of empirical models, using information regarding the sea-level change from different techniques including satellite altimetry and tidal gauges, is not sufficient to capture the complexity of tides across the GBR system (Seifi et al., 2019). Previous studies of shifts in tidal dynamics due to SLR predict moderate to large variations in the tidal cycle, due to the sensitive nature of resonant or near-resonant tidal basins regarding changes in bathymetry (Harker et al., 2019). Therefore, tidal modeling at multiple spatial scales can provide insight into future tidal dynamics as a function of SLR in these complex environments.

This study utilizes an unstructured mesh (spatially-varying resolution) numerical model to predict tidal dynamics on the GBR. We validate the model against tidal gauges in the region and simulate three future scenarios

with 43 cm, 84 and 110 cm of future sea level rise, representing the projected sea levels in 2100. We examine the changes and show that detailed information on the bathymetry is required to obtain accurate assessments of the impacts on tidal dynamics of future sea level rise. The paper first describes the model and set-up. Second, it describes the mesh generation and model construction. Third, the model validation is described and finally, the results and discussion are detailed followed by the conclusions and future work.

2. Methods

2.1. Model Details and Set-Up

Coastal models that represent coastal and oceanic regions can be used to predict any alterations in tidal cycles caused by SLR (e.g., Angeloudis et al., 2018; Baker et al., 2020; Goss et al., 2019; Pickering et al., 2017). In this instance, *Thetis* was employed, which is a finite element based coastal ocean model that implements both 2D and 3D equations (Kärnä et al., 2018). Here, we use *Thetis* to solve the 2D non-conservative form of the non-linear shallow water equations:

$$\frac{\partial \eta}{\partial t} + \nabla \cdot (H_d \mathbf{u}) = 0, \tag{1}$$

$$\frac{\partial \mathbf{u}}{\partial t} + \mathbf{u} \cdot \nabla \mathbf{u} - \nu \nabla^2 \mathbf{u} + f \mathbf{u}^{\perp} + g \nabla \eta = -\frac{\tau_b}{\rho H_d}, \tag{2}$$

where η is the water elevation, H_d is the total water depth, ν is the kinematic viscosity of the fluid, and $\mathbf{u}$ is the depth-averaged velocity vector. The Coriolis term is represented as $f\mathbf{u}^{\perp}$, where $\mathbf{u}^{\perp}$ the velocity vector rotated counter-clockwise over 90º In turn, $f = 2\Omega \sin\zeta$ with Ω corresponding to the angular frequency of the Earth's rotation and ζ the latitude. Bed shear stress (τ_b) effects are represented through the Manning's n formulation as:

$$\frac{\tau_b}{\rho} = g n^2 \frac{|\mathbf{u}|\mathbf{u}}{H_d{}^{\frac{1}{3}}} \tag{3}$$

For time-stepping, a second-order Crank-Nicolson discretization was used with a constant time step of 240 s. We used a 2D approach to ensure the simulations are tractable whilst being able to include large areas of high resolution to capture the effects of tidal inundation over the complex reef and coastal structures.

During low tide, areas of the reef will be exposed. To account for this the calculation of wetting and drying (*WD*) in accordance with Kärnä et al. (2011) was used. The *WD* α parameter was set to 10 to account for the steep slopes in places whilst maintaining numeric stability. The models were implemented following the Galerkin finite element discretization (DG-FEM), using the P1DG-P1DG velocity-elevation finite element pair (Angeloudis et al., 2018; Baker et al., 2020). Discretized equations are solved using a Newton nonlinear solver algorithm using the PETSc library (Balay et al., 2001).

2.2. Mesh Generation and Model Construction

In order to simulate the GBR at a sufficiently high resolution, over a wide enough area to capture change in tidal dynamics, we used a two-dimensional unstructured mesh. Meshes were generated in UTM 56S projection space using contours extracted from digital elevation model (DEM) data to generate ”coastal” boundaries and a forced boundary in the Pacific ocean, away from any shallow areas. The model spans from 144.70 W to 155.32 E, −14.76 N to −25.50 S (Figure 1) with mesh resolution between 400 m and 5 km.

Contours extracted from bathymetric and topographic data are used as coastal boundaries. For simulations with wetting and drying (*WD*) enabled, such that the rise and fall of the tide can inundate the land surface, the 5 m contour was used to create the landward boundary. Where *no-WD* was used, the 0 m contour was used. Boundaries and mesh creation were carried out in QGIS (QGIS.org, 2020), using qmesh (Avdis et al., 2018) and gmsh (Geuzaine & Remacle, 2009). A two-dimensional Delaunay triangulation algorithm was used, with the resolution of the mesh controlled by a number of mesh metrics (see equations). Different unstructured meshes were used for *no-WD* and *WD* simulations. The *no-WD* mesh consisted of 159,912 nodes and 319,908 elements. This mesh was used just for present day simulations with varying drag coefficients for model validation (Section 2.3). The

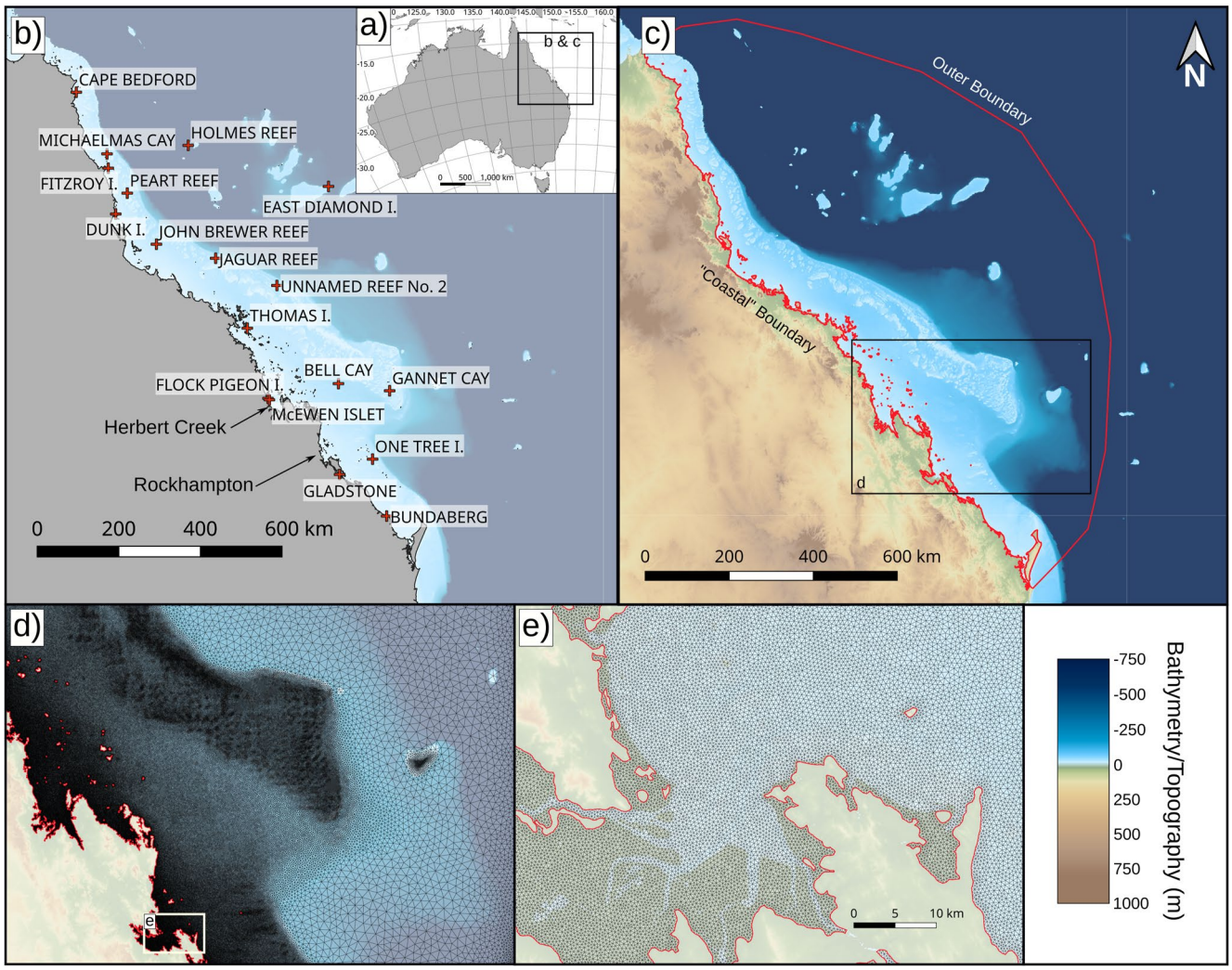

Figure 1. Overview of the modeled domain (a), with details of places named in in the manuscript (b) and the computational domain (c), showing the bathymetry/topography used. Close up of the mesh in the Rockhampton region are shown (d), showing the variation in mesh resolution across the domain, and also indicating where the mesh includes topography up to the 5 m contour (e).

WD mesh consisted of 266,526 nodes and 533,138 elements, reflecting the increased area simulated at high resolution. This was used for the present-day simulation, as well as the 43 cm SLR, 84 cm SLR and 110 cm SLR. Simulations with *no-WD* had a minimum depth set to 6 m to avoid model instability. All runs used a viscosity of 1.0 (Ns/m^2) as well as the use of a "sponge" layer of higher drag and viscosity at the forced boundary; this layer decreased from a value 1,000 times higher than the model value to the model value over a distance of 5,000 m to maintain stability of the model.

Element sizes ranged from 400 m in and around islands and coastlines, up to 5,000 m on the outermost boundary of the mesh. Element size is governed by a number of factors. First, the minimum resolution (400 m) is set on the "landward" boundaries, which then increases away from the shoreline after a distance of 500 m to a resolution of 5 km after 1,200 m away from the boundary (m_c). Second, a similar metric is employed on the forced boundaries with resolution increasing from 2.5 to 5 km over a distance of 100 km from the boundary using a linear increase (m_b). A depth-based metric, m_d, is used whereby a sigmoidal function is used to control resolution according to equation:

$$m_d = 25000\frac{e^{((H_m-500)/150)}}{e^{((H_m-500)/150)}+1} \quad (4)$$

Table 1
Modeling Scenarios Used to Validate the Present Day Model

Number	Name	Drag coefficient	Wetting and drying
1	GBR noWD025	0.025	No
2	GBR noWD03	0.03	No
3	GBR noWD05	0.05	No
4	GBR noWDSVD	0.025–0.25	No
5	GBR WD0.025	0.025	Yes
6	GBR WDSVD	0.025–0.25	Yes

where H_m is max $(h, 6)$ and h is the water depth. Finally, we also employed a metric based on the gradient of depth, m_g, according to equation:

$$m_g = \max(750.0, G) \text{ where} \tag{5a}$$

$$G = 100000 \frac{1}{2.5c} e^{-0.5\left(\frac{7000000 \nabla H_m}{c}\right)^2} \tag{5b}$$

The final mesh metric is then calculated using the minimum of the individual metrics:

$$\min(m_c, m_b, m_d, m_g) \tag{6}$$

The mesh resolution was chosen to be able to capture the movement of the tidal waves (the celerity of which is a function of water depth), but also resolve the complex bathymetry and coastal geometries in and around reefs and islands. Although the implicit nature of the temporal solver means the Courant–Friedrichs–Lewy condition (CFL) can be greater than 1, we have been conservative and ensured that it is less than 1.0 for the given time-step and resolutions. The approach used is similar to that of previous unstructured mesh models of the GBR (Lambrechts, Comblen, et al., 2008; Lambrechts, Hanert, et al., 2008).

Data for the modeling was provided by a range of sources. The bathymetry and topography data consisted of a 100 m resolution DEM of the GBR region (Beaman, 2010). These data were loaded into the model using HRDS (Hill, 2019), which carried out bi-linear interpolation of the DEM data to the mesh. TPXO tidal levels (Egbert & Erofeeva, 2002) were used to force the simulation on the open boundary only. There were 11 tidal constituents used to force the models: M_2, S_2, N_2, K_2, K_1, O_1, P_1, Q_1, M_4, MS_4 and MN_4. No astronomical tidal forcing on the water surface was used. Tidal forcing was updated at each timestep of the model (240 s). The following future sea-level heights were used: 43 cm, 84 and 110 cm, as these scenarios represent the low and high ends of likely future SLR from The IPCC Special Report on the Ocean and Cryosphere in a Changing Climate (Pörtner et al., 2019). Although only two RCP scenarios were used, we took the minimum projection from RCP2.6 which was 43 cm; and the lowest (84 cm) and highest (110 cm) of the RCP8.5 scenario projections. The RCP4.5 and RCP6.0 projections were similar to the RCP2.6 scenario for GMSL, hence the choices made. To increase sea level, the appropriate height was subtracted from the DEM to generate a sea-level rise. There was no attempt to account for any potential morphological changes or changes in coral reef depths due to the short time into the future these simulations represent, nor was the tidal forcing altered for future scenarios.

All models were run from 1st Jan 2000 for 44 days. This includes 14 days spin-up and then a further 30 days for post-simulation analysis. Maps of tidal components were created using Uptide (Kramer et al., 2020) which were then compared to the tidal gauge data from Australian Hydrographic Office (2020) using bespoke python scripts. Statistical analyses of these differences was carried out via a Wilcoxon Signed Rank Test (Woolson, 2008) in R Studio (RStudio Climate Change Initiative Coastal Sea Level Team, 2020).

2.3. Model Validation

Prior to simulating the impact of sea-level rise on future tidal dynamics, the modern day model was validated against empirical data. Here, a number of simulations were performed with and without *WD* and with different drag coefficients to determine how these parameters impacted model accuracy. The drag coefficients are based on those used by Andutta et al. (2012) where a higher Manning's coefficient was used over reef areas than non-reef areas (Spatially Varying Drag - SVD). Manning's coefficients were also tried between those in Andutta et al. (2012) and that of "clean sand" to examine the effects on tidal flow. Locations of reefs were derived from World Resources Institute (2016) and as such the higher drag value was used where reefs are mapped, with the lower value used elsewhere in the SVD simulations. Where only a single value is given, the same value was used across the whole domain. Model accuracy was calculated using 78 tidal gauges (Australian Hydrographic Office, 2020) and by comparisons of the model to FES2014 tidal data (Lyard et al., 2020). A total of six scenarios were modeled for the present day to establish optimal numerical parameters (Table 1).

Table 2
The Pearson's Correlation (R^2) and Standard Error (Std.Error) Calculated for Each Tidal Amplitude for Each of the Model Runs Highlighted in the Previous Table 1 Based on the 78 Tidal Gauges Used in This Study

	R^2				Std. Error			
Run/ constituent	M_2	S_2	K_1	O_1	M_2	S_2	K_1	O_1
GBR noWD025	0.99	0.82	0.87	0.83	0.016	0.140	0.094	0.094
GBR noWD03	0.99	0.65	0.87	0.84	0.018	0.222	0.093	0.092
GBR noWD05	0.97	0.02	0.86	0.83	0.044	0.343	0.105	0.096
GBR noWDSVD	0.98	0.18	0.89	0.84	0.030	0.247	0.051	0.054
GBR WD0.025	0.99	0.94	0.87	0.84	0.013	0.052	0.083	0.077
GBR WDSVD	0.98	0.41	0.89	0.85	0.024	0.139	0.049	0.059

From all six simulations, the best match to tidal gauge and FES2014 data is simulation 5 (Table 2 and Figure 2). M_2 amplitude is consistent across all runs in terms of correlation coefficient, but shows decreases in standard error for runs with WD enabled or with a drag of 0.025. In contrast, S_2 shows large amounts of variation in both correlation coefficient and standard error depending on model parameters. The deviation is highest with a higher or spatially varying drag coefficient, showing the sensitivity of the S_2 component do the drag coefficient. The O_1 constituent shows a marginally better fit to data when wetting and drying is used, as does K_1 and performs best when a spatially varying drag is used. There is little difference spatially of the reconstructions in the M_2 tide between the six simulations (not shown), which is expected due to the consistency of the M_2 statistics shown in Table 2. There are close similarities between the model and FES2014 data with a slightly lower than expected M_2 amplitude in Herbert Creek area toward the coastline compared to the FES2014 data (Figure 2). The K_1 and O_1 tides appear to be spatially similar across the six simulations (not shown), but FES2014 appears to be slightly higher in comparison. We conclude that WD increases the fit to tidal gauge data and that a constant Manning's drag coefficient of 0.025 gives the best overall model performance.

The model shows good agreement to reconstructed water elevations from AusTides (Australian Hydrographic Office, 2020) across the whole GBR. In general, the model slightly over-predicts the maximum/minimum water height from neap to spring, and then slightly under-predicts from spring to neap (Figure 3). Some places show a slight shift of phase, e.g. Thomas Island (Figure 3) of less than 15 min (the output frequency of the model is 15 min), but overall even complex tidal signals, such as that at Michaelmas Cay, are reproduced well. Given the spatial match to FES2014, the high Pearson correlation to tidal gauge amplitude data and good comparison to water elevations, we are confident that the model is reproducing the tidal dynamics of the GBR system.

3. Results and Discussion

The future sea-level scenarios are compared to the present sea-level. The M_2 and S_2 constituents, and tidal range variations are the primary focus. The K_1 and O_1 constituents are included to examine and account for the variations in the semidiurnal and diurnal tides across the northern and southern sector (see supplementary information). The semidiurnal constituents display changes in amplitude from the present-day across each of the SLR simulations by both examining the spatial changes and the tidal gauge data.

The M_2 amplitude displays spatial variability across the whole domain (Figure 4). The general trend is for a reduction in M_2 amplitude with increasing sea-level rise. However, there is a small increase in M_2 amplitude north of Herbert Creek in both the 43 and 84 cm scenarios. This disappears in the 110 cm scenario, and the small increase is pushed further north. The largest decreases are in the central and southern sections of the reef where the gap between the outer reef and the coastline is largest. There is little change in the phase, except a subtle shift of the phase line north of Herbert Creek, which moves northwards in the 110 cm scenario. These decreases in amplitude correspond to where the amplitude is highest. In contrast, the S_2 amplitude displays increased amplitude across each of the SLR simulations with a small decrease toward the southernmost area of the simulation around Bundaberg. There are subtle changes to the phase contours, particularly just north of Herbert Creek where a slight decrease in S_2 amplitude occurs in the 84 cm scenario, but this is reversed in the 110 cm scenario.

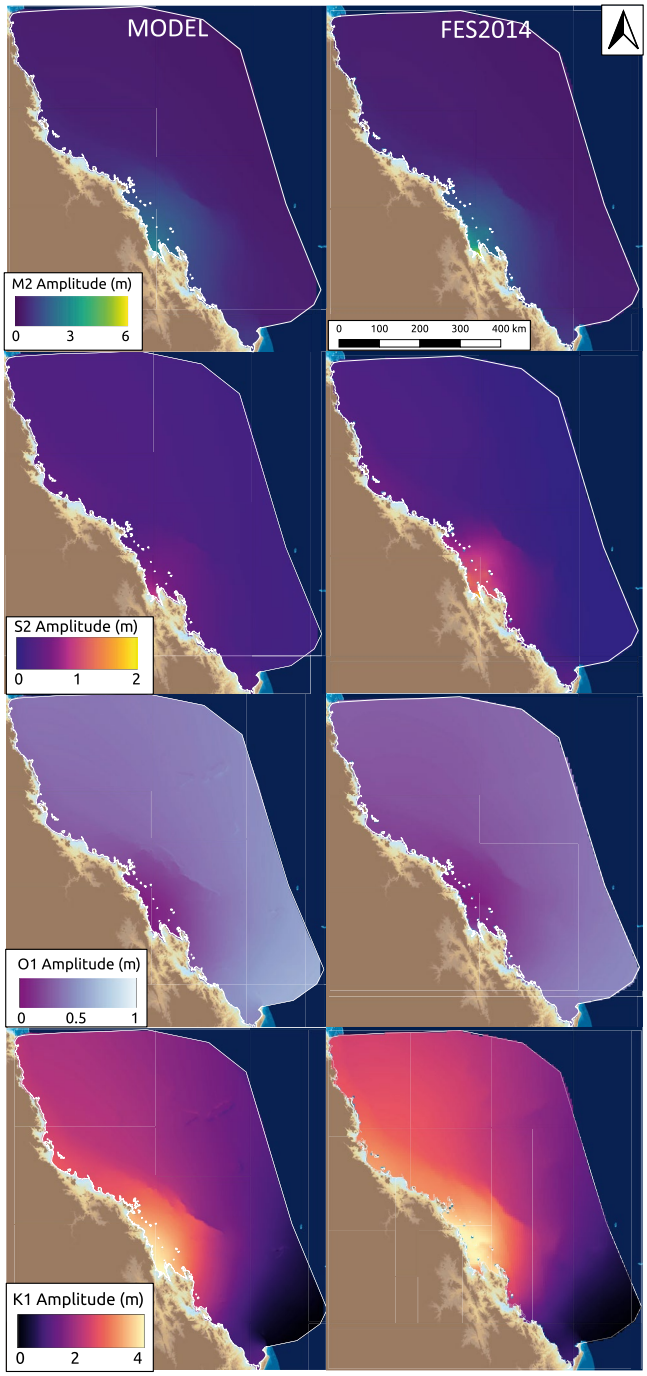

Figure 2. Comparison between the present-day run 5 model simulation output (left) and FES2014 data (right) across each tidal amplitude, M_2, S_2, O_1 and K_1 (top to bottom).

There are similar changes for the O_1 and K_1 components (Figure 5). K_1 shows a reduction in amplitude in a similar manner to the M_2 components, with larger decreases of amplitude in the Herbert Creek region. The O_1 components shows very little change and only very small localized changes, both positive and negative, in amplitude. Overall, the combined changes in amplitude result in a clear north-south divide in shifts to the tidal amplitude (Figure 6). There is a clear dividing line to the north of Herbert Creek. South of this line, where present day tidal range is highest, there is a reduction in tidal range and the magnitude of that reduction increases with sea-level rise. Conversely, north of this line, there is an increase in tidal range, which again has a greater magnitude as sea level rises. In the far north of the reef there is a localized decrease in tidal range, the magnitude of which, again, increases as sea level rises. The tidal range on the outer edge of the reef also increases slightly as sea level rises. The model results display changes in tidal range up to 10 cm, which is around 10% of the total sea-level rise simulated.

The modeled gauges reflect the large-scale spatial variations observed from the model. Plotting the amplitude at each gauge shows the range of amplitudes measured at each tidal gauge in the model (Figure 7). The K_1 and O_1 components show very little change, with K_1 reflecting the slight decrease shown in the spatial results, whereas as O_1 shows a slight increase with the 43 cm scenario, but then slight decreases with higher sea levels. As shown in the previous spatial plots, the M_2 constituent shows relatively steady (and non-significant) slight decrease at 43 and 84 cm SLR, but then a significant decrease at 110 cm SLR. In contrast S_2 shows very little change at 43 and 84 cm SLR (84 cm SLR differences are, in fact not significant), but a significant increase in tidal amplitude at 110 cm SLR across the modeled gauges. The modeled gauges therefore reflect the spatial changes and trends well, and show the significance of the impact of SLR.

We can examine the impact of SLR at the tidal gauge location in more detail. Some tidal gauge locations show very little difference, 0.0075 m total reduction in tidal range under the 110 cm of SLR scenario on an original tidal range of over 2 m; a 0.3% difference (Michaelmas Cay) (Figure 8). Others show a much larger alteration; Bundaberg shows a 0.8 m change under the SLR110 scenario. At all sites where a difference is observed, the magnitude of the difference increases with increasing sea-level rise. Moreover, the changes in tidal elevations at the tide gauge locations exhibit a range of behaviors (Figure 8). Some show only a very small difference (order millimeters) which varies with tidal cycle, but is largely consistent across the neap-spring cycle at all sea level rises (e.g., Fitzroy Reef - not shown). However, at 110 cm sea level rise almost all tide gauge sites show a shift in the neap part of the tidal cycle; shown by the increase in the green line in Figure 8 after day 24. The size of this shift varies across the domain. In some places it is still at centimetre-scale (e.g., One Tree Island), in others the shift leads to a significant change in the timings of the low and high water points (e.g., Thomas Island), which is shown by the differences being shifted compared to modern day elevations (Figure 3). There is a relationship of the behaviors from north to south, with tidal gauges in the northern section of the GBR generally showing fewer shifts in elevations and timings. Where the tidal range is altered significantly, there is a general trend for an increase of the neap section of the tidal cycle being the driver for this change (i.e., a reduction in the tidal range).

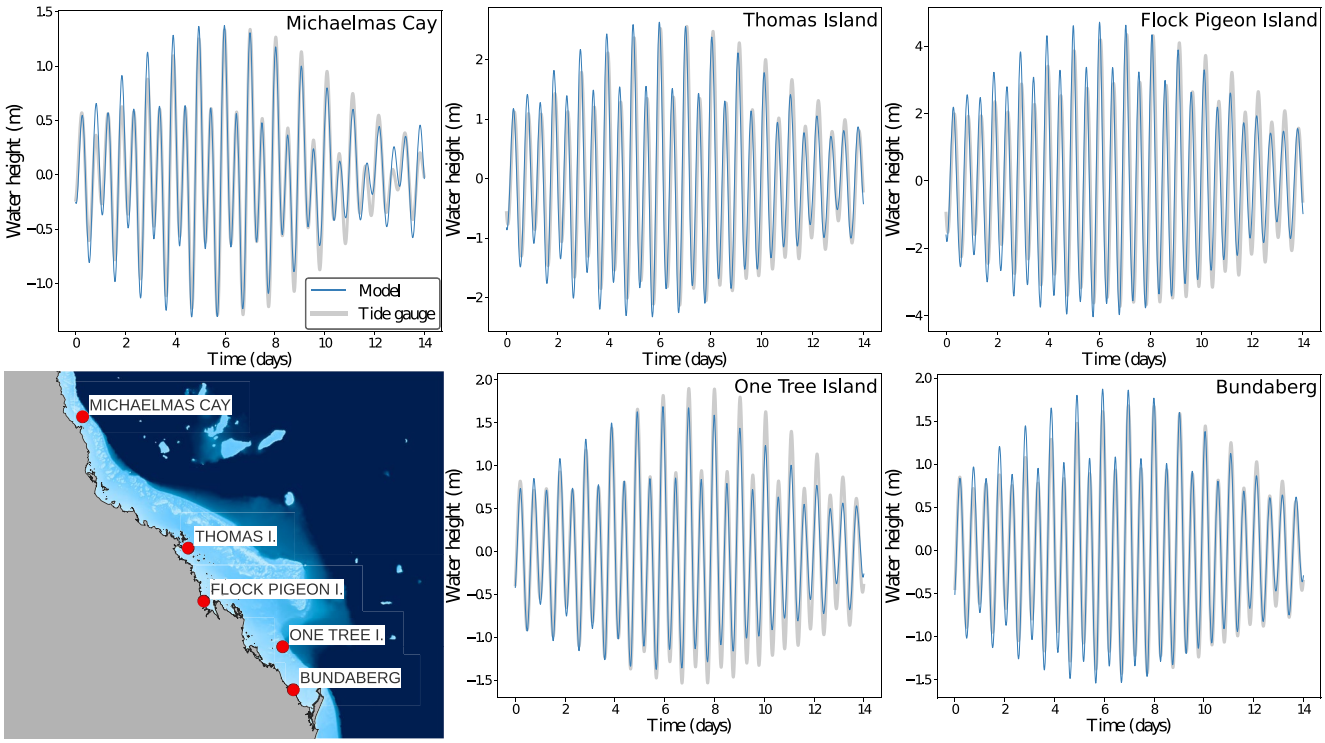

Figure 3. Comparison of modeled water elevations (blue) to reconstructed water elevations from the AusTide data (Australian Hydrographic Office, 2020) (gray) from north to south on the GBR. The model reproduces the reconstructed water elevations across the GBR system.

3.1. The North-South Divide

Eight gauge locations were selected out of the 78 simulated that cover the shift from a positive tidal range change in the southernmost area to the negative change in northern areas, as well as examine changes offshore compared to coastal locations (Table 3). Offshore reef locations (East Diamond Island - point 3 and Holmes Reef - site 11)

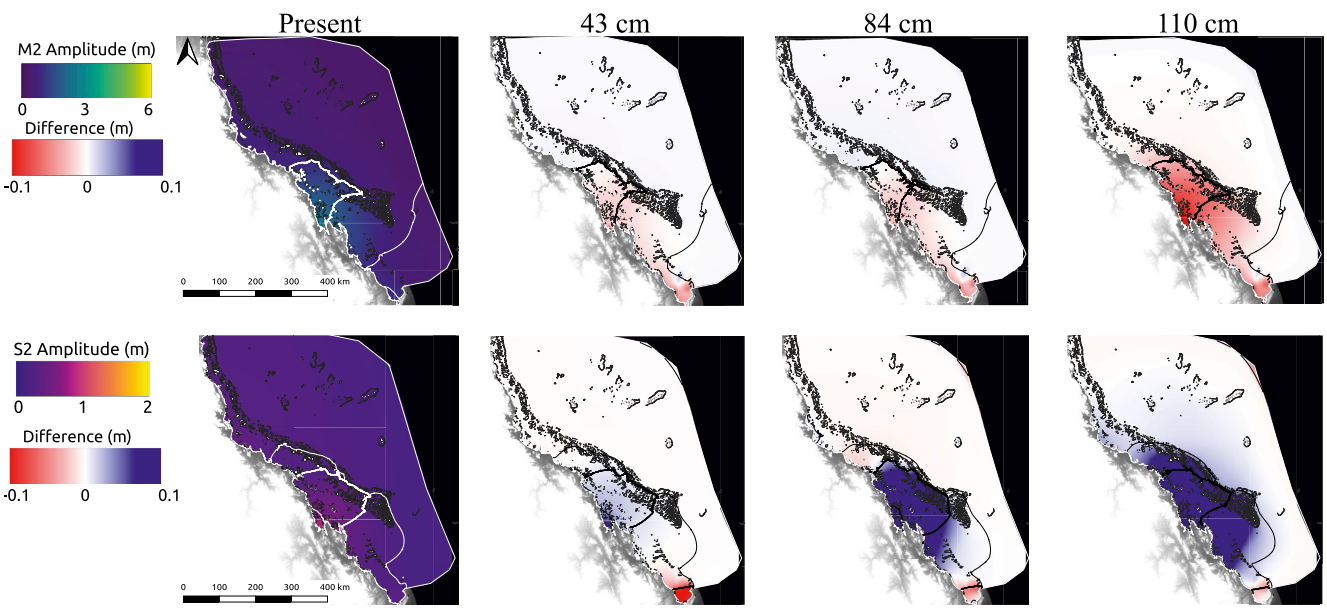

Figure 4. The effect of sea-level rise on the M_2 amplitude (top) and S_2 amplitude (below) across 43 cm, 84 and 110 cm simulations compared to the present-day. Amplitude is measured in meters (m) and the contour indicates the phase.

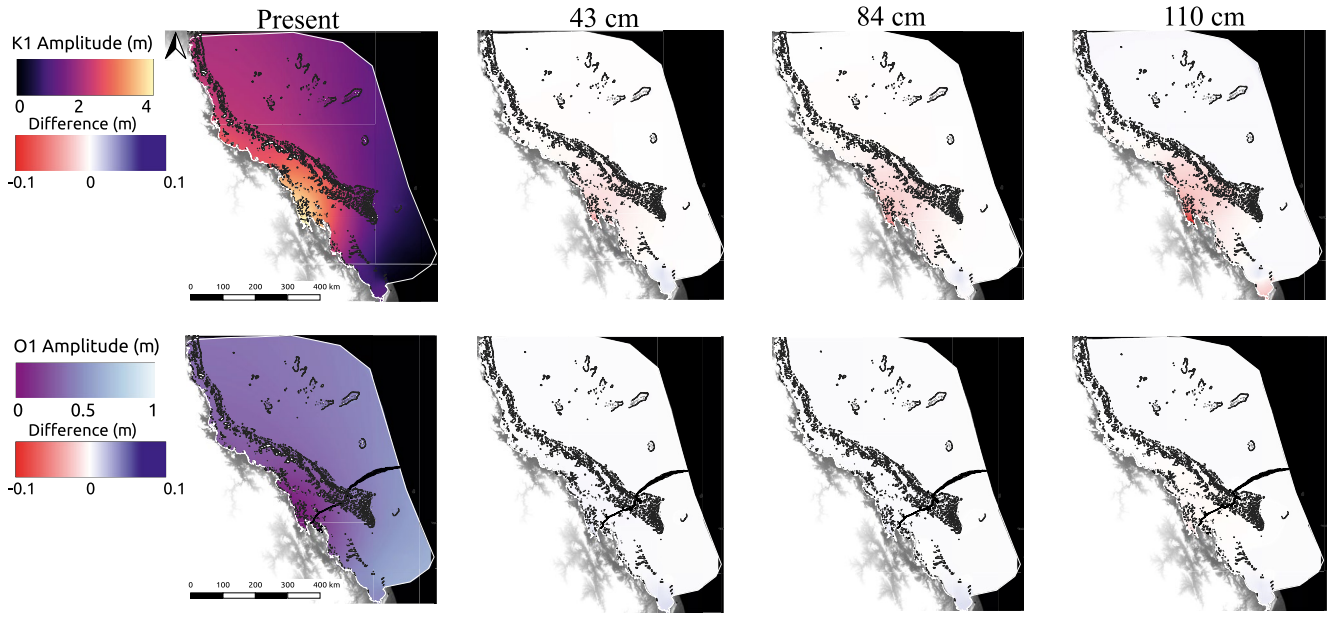

Figure 5. The effect of sea-level rise on the K_1 amplitude (top) and O_1 amplitude (below) across 43 cm, 84 and 110 cm simulations compared to the present-day. Amplitude is measured in meters (m) and the contour indicates the phase.

show very little change, with percentage differences of 1% or less. Offshore sites on the GBR itself such as Jaguar Reef (point 36) show slightly large percentages differences of up to 2% in S_2. Point 47 (Thomas Island), a coastal site, in a similar position in the north-south divide as Jaguar Reef shows a much larger shift in the S_2 constituent of 46% for a 110 cm SLR.

Focusing on the southern region, across the three SLR simulations M_2 amplitude decreases at McEwen Islet (60) by −5.26%. M_2 decreases are greater in the 110 cm simulation with 43 and 84 cm appearing similar (Table 3). However, the S_2 component has a much larger percentage increase of nearly 50%. Sites below the Capricorn Channel entrance in the far south of the GBR, such as One Tree Island (73) displayed the smallest variation across each simulation, but still around a 15% increase in S_2 amplitude, but around 1%–2% decrease in M_2 amplitude. O_1 shows a positive difference of 3.18% at McEwen Islet (site 60) with 43 cm SLR which decreases to −4.57% difference from the present-day at 110 cm. K_1 amplitude displays large differences toward McEwen Islet (60) with −21.3% at 110 cm SLR (Table 3), but these are small changes in absolute terms. One Tree Island (site 73) displays a small percentage difference for the diurnal constituents. Overall, the changes in S_2 and M_2 dominate, resulting in tidal range changes of around 2%, but reducing to 0.6% south of the Capricorn Channel (One Tree Island - site 73).

In the northern region, the changes are generally minimal. Peart Reef (site 19) shows very low percentage changes as does Cape Bedford (site 7). These changes are similar to those seen on reef locations in the south (e.g., Jaguar Reef). At Peart Reef there is a change of behavior when SLR reaches 110 cm with the M_2 change switching from positive to negative and S_2 showing the reverse behavior. Cape Bedford does not show this behavior. The diurnal constituents in this region show similarly small changes. As a result the changes in tidal range are also small with either small negative (Cape Bedford - site 7 and Peart Reef - site 19) on the reef itself or small positive difference (Holmes Reef - site 11) offshore. Note that the spatial variation confirms this, with spatially varying small positive and negative differences in the northern sector (Figure 8).

Six gauge locations were selected to depict variations in the tidal ellipses of the M2 and S2 amplitudes (Figure 9). Northern gauge locations displayed little change in tidal ellipses of the M2 amplitude (Holmes Reef - site 11 and John Brewer Reef - site 33). There was a slight change at High Island (site 17) with a shift more toward the north and south in the 110 cm scenario. Flock Pigeon Island (site 59) changed toward north and south from 84 to 110 cm which is similar to High Island. High Peak Island displayed a change toward north-east and south-west at 110 cm where other simulations were closed to east and west. One Tree Island (site 73) had little changes in

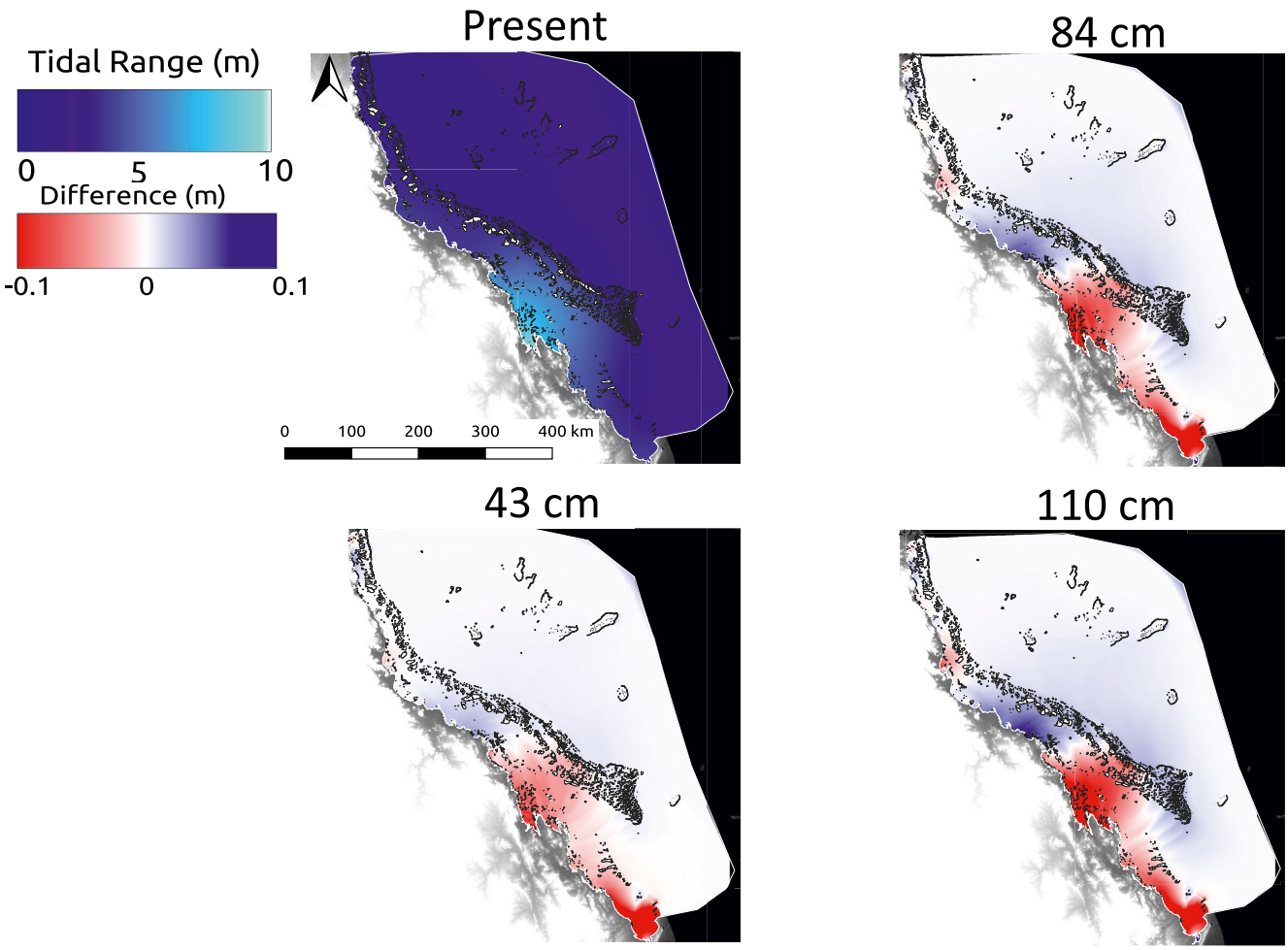

Figure 6. The effect of sea-level rise on tidal range across the 43 cm, 84 and 110 cm simulations compared to the present-day. Tidal range is measured in meters (m).

the M2 ellipses which is similar to the northern gauges. The central sector (site 59 and 64) exhibited the greatest changes in the M2 tidal ellipses.

3.2. Tidal Changes

The results display that SLR has an impact on the semidiurnal constituents toward the central and southern GBR with a majority of gauge locations displaying an increase in S_2 amplitude but a decrease in M_2 amplitude (Figure 4). These changes in S_2 and M_2 are result in a north-south divide of tidal range changes (Figure 6). Spatially, each of the gauge locations respond differently which is related to regional variations due to the flow of water across the reef (Harker et al., 2019). Changes appeared to be especially higher toward Herbert Creek (Figure 4), where Flock Pigeon Island (59) and McEwen Islet (60) are located, and toward the southern part of the domain from Rockhampton toward Gladstone and Bundaberg (Figure 1). The opposing changes in the S_2 amplitude and M_2 amplitude revealed in this study could be linked to natural oscillation. As the S_2 increases the natural period of oscillation is moving away from the M_2 amplitude, in which a decrease is observed (Pickering et al., 2012). The phase changes for S_2 and M_2 (Figure 4), confirms this, with opposing changes of expansion or contraction of phase contours within the Capricorn Channel. Opposites in these constituents can lead to an increase or reduction on the effect of the spring tidal amplitude but an increase or reduction on the neap tidal amplitudes (Pickering et al., 2012). Here, we see a general increase in the neap tidal amplitude, but both increases and decreases in the spring tidal amplitude, depending on location (Figure 8). The increase in neap tide amplitude seems to occur across most of the GBR, except the far south (Bundaberg) and is shown by the tidal elevation difference increase post 24 days (Figure 8). Most sites also show an increase in amplitude or a slight tidal phase

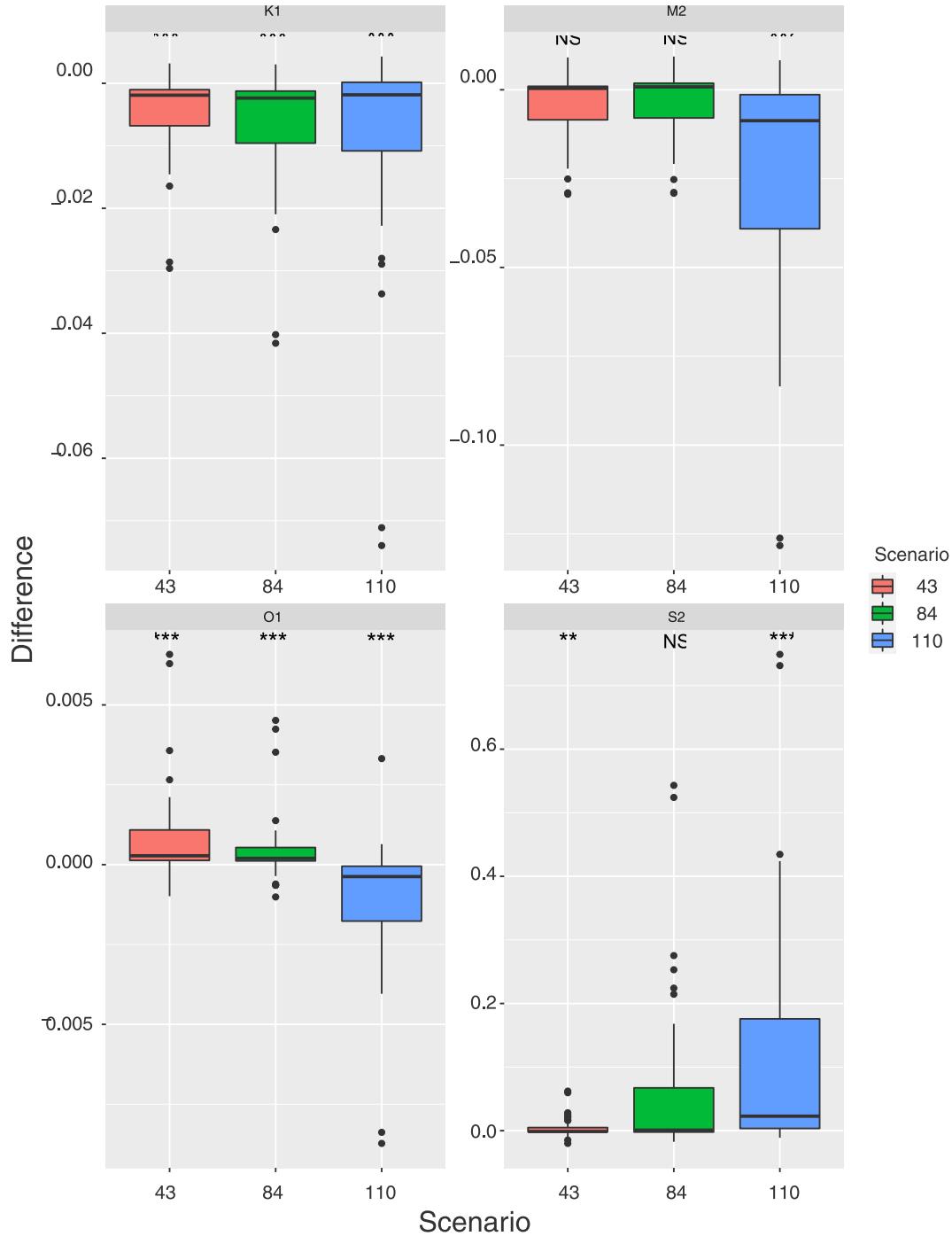

Figure 7. The amplitude difference (m) for the three sea-level rise scenarios (43 cm, 84 cm, and 110 cm), compared to the present-day tidal constituents for the 78 modeled gauge locations. Significance is shown by codes in order of: *** <0.001, ** <0.01, * <0.05, and >0.05 by No Significance (NS). The box plots display the range of amplitude difference with some points lying outside the desired range.

shift through most of the tidal cycle. However, Michaelmas Cay shows only a very small change (to 0.0075 m over a tidal range of nearly 2m–0.3% change), but Bundaberg shows a +/- 0.8m change over a tidal range of nearly 3 m (25% increase) for SLR110. Conversely, One Tree Island shows a largely negative change over the spring tidal cycle, but a large positive change over the neap only, but only under SLR110. At nearly all sites we see the maximum change occurring in the SLR110 scenario. We therefore conclude that rising sea-level can potentially

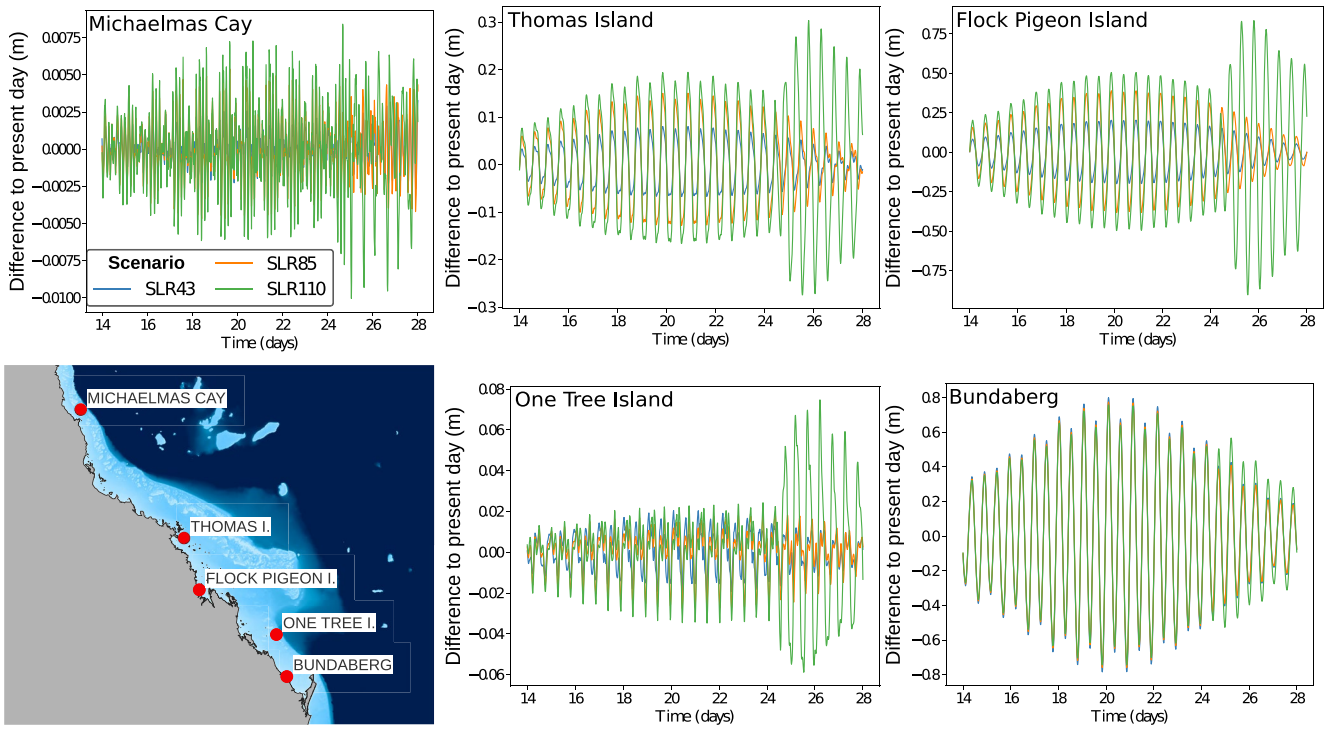

Figure 8. Modeled gauge elevation plots for selected locations as shown in Figure 3. Plots show the difference (m) between the future scenarios (SLR43, SLR85, SLR110) to modern day elevations for a 14 day window between day 14 and 28 to capture the full neap and spring cycle. Some locations show a substantial difference to the present day, especially around the neap tide. See text for details.

increase the both neap and spring tidal range and potentially raise the tidal range average which can lead to increases in risk of flooding due to storm surges or changes in sediment deposition (Pickering et al., 2012, 2017). Here, we see a similar effect to that described by Pickering et al. (2012), where a number of sites show larger shifts at the neap part of the tidal cycle, but the then depending on where the site is located in the north-south direction would see a decrease in spring tidal range (south), little or no change (north of Herbert Creek) and a decrease in spring tidal range (in the northern section of the GBR). This shift matches the flow patterns depicted by the tidal ellipses (Figure 9). In the southern sector of the GBR the M_2 tidal ellipse shows a small decrease in velocity whereas S_2 shows an increase (57: Gannett Cay) or a rotation in direction (59: Flock Pigeon Island and 56: Bell Cay). In the central sector, there is very little change to both M_2 and S_2 constituents (33: John Brewer's Reef). The northern sector hows a very small decrease in S_2 ellipse velocities, but a very small increase in M_2 (12: Michaelmas Cay).

To explain this variation we hypothesize that the raising sea-level reduces the bed friction (as friction is a function of water depth, e.q. 3). This in turn then alters the coupling of the oceanic waters to the shelf water as shown by Arbic and Garrett (2010) in hypothetical simulations. The presence of a complex, shallow barrier reef system between the ocean and continental shelf may complicate this further or enhance the effect. Previous work on tidal changes due to sea-level change put forward the idea that tidal components become correlated (tidal anomaly correlation – TAC), which may also explain the coupled changes of S_2 and M_2 seen here (Devlin et al., 2017). Regardless, more work is required to understand how these changes are correlated.

In contrast to the semi-diurnal constituents, the diurnal constituents show little or no change. The O_1 amplitude and phase display little difference with changes in SLR, whereas the K_1 amplitude displays a small decrease toward the central sector if the GBR, especially in Herbert Creek, and a slight increase toward the southern sector near Bundaberg (Figures 1 and 5). The K_1 phase is only present as a significant constituent in Herbert Creek in the present-day. This is largely due to the K_1 phase amphidromic point being outside the simulated domain. Other studies that have been conducted globally or across a larger domain have shown that K_1 appears to show the largest differences in Asia (Pickering et al., 2017), or it is governed by a single amphidromic point in the Gulf of Carpentaria off the coast of the Northern Territory, Australia (Harker et al., 2019). The present study did not

Table 3
Absolute Values and Percentage Differences of Key Tidal Constituents and Tidal Range at Selected Tidal Gauge Locations

Gauge location		Present day	%D: 43 cm	%D: 84 cm	%D: 110 cm	Amp (m): 43 cm	Amp (m): 84 cm	Amp (m): 110 cm
East Diamond Island (3)	M_2	0.42	0.17	0.23	−0.23	0.42	0.42	0.41
	S_2	0.22	−0.56	−1.12	−0.02	0.22	0.22	0.22
	O_1	0.14	0.03	0.02	−0.04	0.14	0.14	0.14
	K_1	0.28	−0.28	−0.31	0.28	0.28	0.28	0.28
	TR	2.18	0.09	0.16	0.19	2.18	2.18	2.18
Cape Bedford (7)	M_2	0.52	−0.37	−0.35	−0.63	0.52	0.52	0.52
	S_2	0.30	−3.75	−3.04	−1.51	0.30	0.30	0.30
	O_1	0.15	−0.55	−0.44	−0.93	0.15	0.15	0.15
	K_1	0.31	−0.63	−1.00	−1.50	0.31	0.31	0.31
	TR	2.65	−0.54	−0.59	−0.61	2.64	2.64	2.64
Holmes Reef (11)	M_2	0.50	0.15	0.21	−0.16	0.50	0.50	0.50
	S_2	0.28	−0.49	−0.80	−0.02	0.28	0.28	0.28
	O_1	0.15	0.08	0.08	0.01	0.15	0.15	0.15
	K_1	0.30	−0.24	−0.27	0.28	0.30	0.30	0.30
	TR	2.56	0.03	0.05	0.06	2.56	2.56	2.56
Peart Reef (19)	M_2	0.57	0.17	0.28	−0.29	0.57	0.57	0.57
	S_2	0.32	−0.51	−0.55	1.75	0.32	0.32	0.32
	O_1	0.15	0.10	0.11	−0.10	0.15	0.15	0.15
	K_1	0.31	−0.37	−0.50	−0.25	0.31	0.31	0.31
	TR	2.80	−0.03	−0.14	−0.22	2.79	2.79	2.79
Jaguar Reef (36)	M_2	0.61	0.30	0.47	−0.85	0.61	0.61	0.61
	S_2	0.30	−0.66	−2.64	3.31	0.30	0.30	0.31
	O_1	0.15	0.14	0.12	−0.05	0.15	0.15	0.15
	K_1	0.31	−0.36	−0.42	0.10	0.31	0.31	0.31
	TR	2.88	0.21	0.42	0.54	2.88	2.89	2.89
Thomas Island (47)	M_2	1.39	−0.55	−0.48	−4.41	1.39	1.39	1.36
	S_2	0.34	3.47	25	46.19	0.34	0.39	0.48
	O_1	0.18	0.77	0.30	−1.79	0.18	0.18	0.18
	K_1	0.37	−2.71	−3.77	−5.74	0.36	0.36	0.36
	TR	5.29	−0.16	−0.17	−0.24	5.29	5.29	5.28
McEwen Islet (60)	M_2	2.57	−1.16	−1.15	−5.26	2.55	2.55	2.50
	S_2	0.80	7.2	40.4	48.3	0.83	1.07	1.18
	O_1	0.19	3.32	2.30	−4.77	0.19	0.19	0.19
	K_1	0.41	−7.87	−11.4	−22.3	0.39	0.38	0.37
	TR	8.85	−0.92	−1.58	−1.96	8.81	8.78	8.77
One Tree Island (73)	M_2	0.81	−1.03	−0.94	−1.97	0.81	0.81	0.81
	S_2	0.26	−1.43	6.04	15.0	0.26	0.27	0.29
	O_1	0.13	0.21	0.16	−0.30	0.15	0.15	0.15
	K_1	0.26	−0.85	−0.86	−0.64	0.26	0.26	0.26
	TR	3.06	−0.70	−0.64	−0.63	3.05	3.05	3.05

Note. TR - tidal range. %D - percent difference.

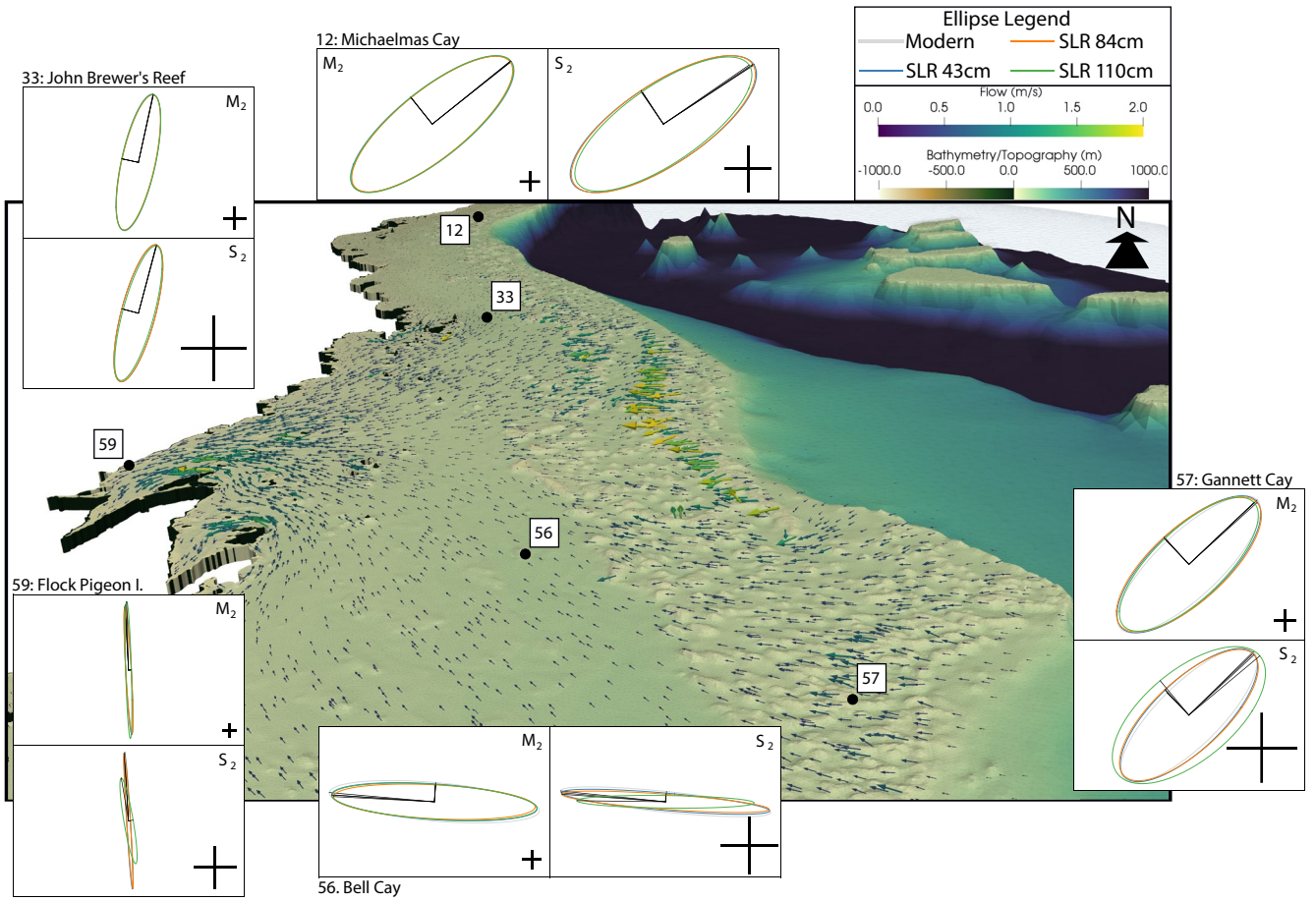

Figure 9. Oblique 3D view of the GBR looking north (center) with selected locations showing both M_2 and S_2 tidal ellipses. Arrows in central figure show tidal flow during peak flood, with rapid flow over the central Capricorn Bunker and into Herbert Creek. Crosses in each plot show 0.1 m/s flow, except for site 12, Michaelmas Cay, which show 0.025 m/s. Colors on ellipses correspond to the modeled scenario, with black lines showing the real and imaginary axes. See text for discussion on tidal ellipses.

cover this region. The larger changes in K_1 are found across the reef and toward the coastline where waters are shallow this could be related to a decrease in bottom friction as a result of SLR or resonant effect change (Kuang et al., 2017).

The tidal range displays a spatially variant behavior across the simulated domain. Although changes appear relatively small around +/-1% in some instances, this is equivalent to a 10% increase or decrease of maximum SLR scenario. This is similar to observations by Pickering et al. (2017), they observed changes at coastal cities, whereas this study witnessed a general difference in tidal range at gauges located both at coastal and reef locations. Offshore islands exhibited little difference. SLR appears to have a greater implication on coastal gauges compared to gauges which are located away from the coast. Increases in tidal range across reefs promote increases in shoreline energy meaning SLR could significantly increase wave energy onto coastal regions and shorelines (Péquignet et al., 2011). SLR promotes increases in wave action and extreme weather events which lead to loss of infrastructure and ecosystems as well as coastal recession and flooding (Green, 2010; Pickering et al., 2017). Many of Australia's major cities are situated on the eastern coastline, which increases the likelihood of exposure to these risks. The observed changes in tidal range may also contribute to these changes (Church & White, 2006; Pelling & Green, 2014; Péquignet et al., 2011).

Previous studies on the impact of SLR on tidal processes around Australia have taken a regional approach, modeling the whole continent (Harker et al., 2019). Similar to this study, Harker et al. (2019) use a 1 m SLR and examined the tidal changes from that rise. They find the opposite results to what is shown here, in that a 1 m SLR produces an increase in M_2 amplitude over the whole GBR region of up to 0.1 m. Unfortunately, that study did

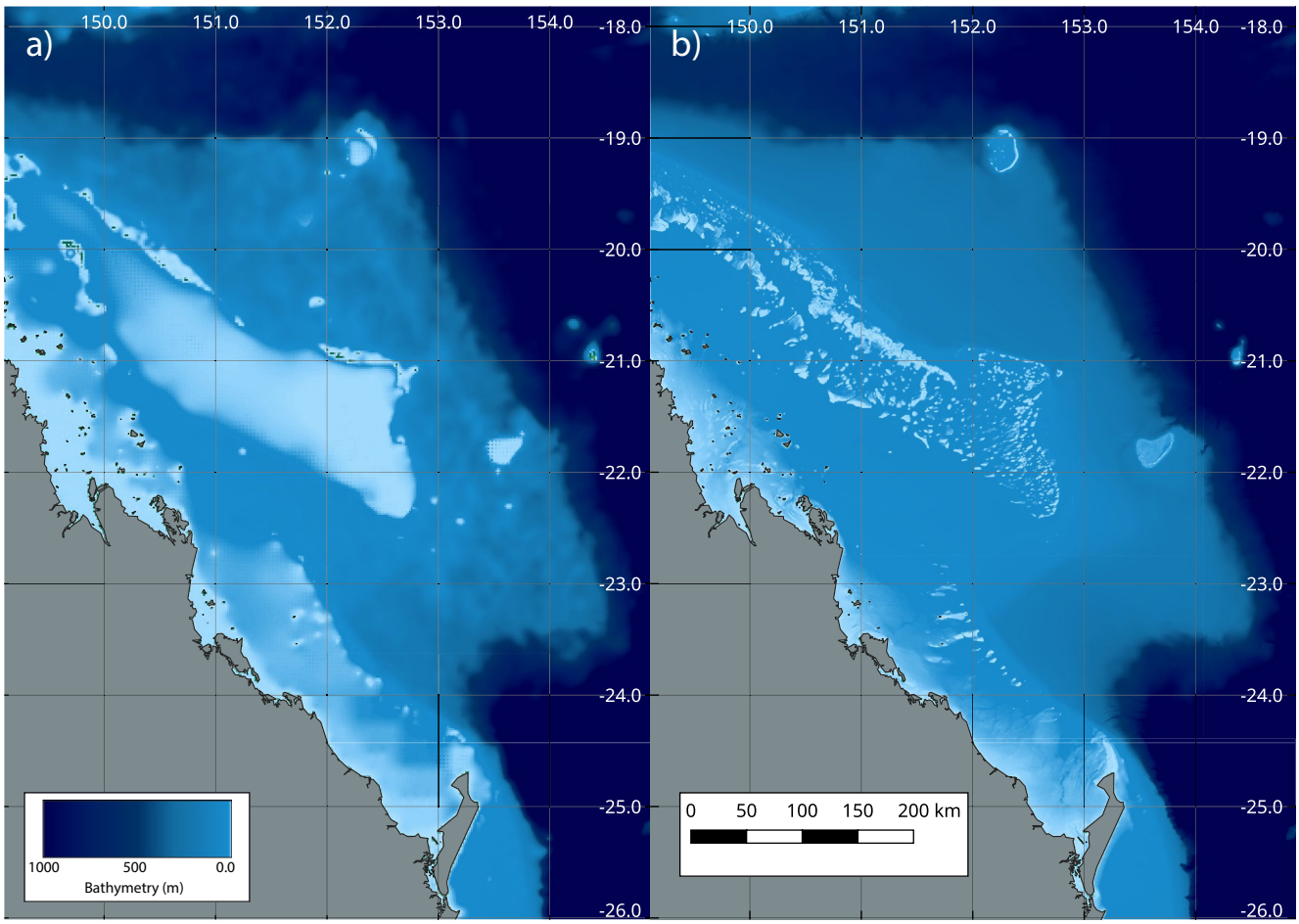

Figure 10. Comparison of bathymetric detail from ETOPO (National Centers for Environmental Information (NCEI), 2009) as used in Harker et al. (2019) (left) and Beaman (2010) as used in this study (right). Note the wide, shallow shelf that forms the Capricorn Bunker in the ETOPO1 data, which in the high resolution data is a network of reefs and deeper channels.

not show the S_2 component. For the K_1 tidal component, Harker et al. (2019) shows no difference, whereas here, we show a small decrease in amplitude. We attribute this difference to the detail of the bathymetry used. Harker et al. (2019) used the the ETOPO1 data set (National Centers for Environmental Information (NCEI) (2009) which shows the GBR as a wide, shallow seaway due to the low resolution compared to the 100 m resolution data (Beaman, 2010) used here (Figure 10). This shows the impact of the complex bathymetry of coral reef systems has on the propagating tidal wave, with regions of deeper channels, missing from the the global data set, giving rise to more complex flow patterns. This result shows the impact of using detailed bathymetric data in regions of high bathymetric complexity.

Overall, we attribute the changes observed to alterations in the tidal signal on and around the GBR to the alterations to the tidal wave as it passes over the GBR in the central and southern sections. The changes occurs due to how the wave interacts with the complex, shallow bathymetry, which shows a large change in the tidal currents once sea-level rise is over 1 m. Further, small-scale, interactions with bathymetry also occur in the Capricorn Channel itself. As sea level rises, the effective drag on the tidal wave decreases, such that with 110 cm SLR, the tidal range is small enough that there is no prolonged exposure of the reef tops and hence drag is drastically reduced. The speed at which the tidal wave traverses the reef impacting the interaction of the diurnal constituents, particularly S_2 in the central/southern region and M_2 in the central/northern sections. The interaction of the two main tidal constituents produces a clear north-south divide in changes to tidal range (Figure 9). As sea-level rises, it will therefore have an effect on the coastal flooding risk, due to changes in tidal range, as well as affecting the flow dynamics over the reef which are an important part of the distributions of nutrients and coral spore and larvae.

3.3. Model Limitations

There are limitations to this study. The future SLR simulations do not account for any changes in coastal geomorphology and ocean basin changes that would occur as sea-level changes (Collins et al., 2018), but also we do not change the external forcing as per Harker et al. (2019). The use of a constant drag coefficient across the GBR will alter the estimations of tides across the GBR. A previous study found that high-resolution models coupled with spatially varying drag largely contribute to accurate estimates of tidal constituents across this region (Seifi et al., 2019). However, here, we found a better match to present-day gauge data with a constant drag coefficient. This requires further investigation, which is beyond the scope of this paper, but should take into account bed sediment type as well as reef versus non-reef environments (Rasheed et al., 2020).

The uniform sea-level applied here may have some impact on the results. There is some spatial variability in sea-level changes around the GBR as detected by the Jason satellite mission (Climate Change Initiative Coastal Sea Level Team, 2020) and differing rates of subsidence along the eastern Australian coast (Hammond et al., 2021). However, this was beyond the scope of this work, but should be included in future work.

The relatively short simulations times of 30 days post-spin-up time was dictated by computational limitations. However, to assess the impact of running a model for this length of time, the modern and 110 cm SLR scenarios were run for a total of 90 days including spin-up. The results indicate the model is stable in running over a three-month period and continues to match tide gauge data well (supplementary information). Moreover, the comparison of the 110 cm SLR scenario continues to show differences that vary with the complex neap-spring cycle seen on the GBR; the complexity of which is in part due to the complexity of the bathymetry (Wolanski et al., 2003).

Finally, the tides were forced via boundary elevation changes only. The domain here was restricted to ensure that astronomic forcing wasn't required, as shown by the model validation, however, including astronomic forcing may improve the validation further and change the details of the results presented here, but not the overall conclusions. In addition, using boundary forcing from global tidal models that have incorporated future sea-level rise scenarios may also be included in future work to assess uncertainties in the changes in future tides in this region.

4. Conclusions

Future SLR will impact the tidal dynamics of the GBR. The GBR displays spatial variation across the system with different processes influencing tidal changes. This paper used high-resolution data via the ocean-coastal model, *Thetis*, to compare present-day sea-level against future SLR scenarios. The use of high-resolution allowed for the examination of the effects of bathymetry on the tides as well as allowing the identification of any observations that would not be visible at a lower resolution, as per previous studies. The semidiurnal tides (S_2 and M_2) were significantly affected with the diurnal tides (O_1 and K_1) showing the least change in absolute terms. Tidal range displayed $\pm$10% change as a proportion of SLR, but this was also spatially variant. These change also altered the neap-spring tidal cycle, with the neap part of the tidal cycle showing a large increase in tidal range.

The changes demonstrated here are significant in places, particularly under a 110 cm SLR scenario. Management schemes should consider both tidal elevation and extreme weather events in order to protect coastlines and infrastructure for future SLR. Furthermore, thought should be given into the effects on coral reef ecology. Management and mitigation must conserve the reef ecosystem; otherwise SLR could significantly reduce biodiversity on reefs, due to both the sea level rise itself, but also the subsequent changes to the tidal dynamics.

Data Availability Statement

All processed model output generated by this work can be found at https://doi.org/10.6084/m9.figshare.15052272.v1.

Acknowledgments
Project formed part of EEM's MSc dissertation. The authors thank two anonymous reviewers for their comments. This project was undertaken on the Viking Cluster, which is a high performance compute facility provided by the University of York. The authors are grateful for computational support from the University of York High Performance Computing service, Viking and the Research Computing team.

References

Al-Nasrawi, A. K., Hamylton, S. M., Jones, B. G., Hopley, C. A., & Al Yazichi, Y. M. (2018). Geoinformatics vulnerability predictions of coastal ecosystems to sea-level rise in southeastern Australia. *Geomatics, Natural Hazards and Risk*, *9*(1), 645–661. https://doi.org/10.1080/19475705.2018.1470112

Andutta, F. P., Kingsford, M. J., & Wolanski, E. (2012). 'Sticky water' enables the retention of larvae in a reef mosaic. *Estuarine, Coastal and Shelf Science*, *101*, 54–63. https://doi.org/10.1016/j.ecss.2012.02.013

Angeloudis, A., Kramer, S. C., Avdis, A., & Piggott, M. D. (2018). Optimising tidal range power plant operation. *Applied Energy*, *212*, 680–690. https://doi.org/10.1016/j.apenergy.2017.12.052

Arbic, B. K., & Garrett, C. (2010). A coupled oscillator model of shelf and ocean tides. *Continental Shelf Research*, *30*(6), 564–574. https://doi.org/10.1016/j.csr.2009.07.008

Australian Hydrographic Office. (2020). AusTides.

Avdis, A., Candy, A. S., Hill, J., Kramer, S. C., & Piggott, M. D. (2018). Efficient unstructured mesh generation for marine renewable energy applications. *Renewable Energy*, *116*, 842–856. https://doi.org/10.1016/j.renene.2017.09.058

Baker, A. L., Craighead, R. M., Jarvis, E. J., Stenton, H. C., Angeloudis, A., Mackie, L., et al. (2020). Modelling the impact of tidal range energy on species communities. *Ocean & Coastal Management*, *193*, 105221. https://doi.org/10.1016/j.ocecoaman.2020.105221

Balay, S., Buschelman, K., Gropp, W. D., Kaushik, D., Knepley, M. G., McInnes, L. C., et al. (2001). Petsc.

Beaman, R. J. (2010). 3DGBR: A high-resolution depth model for the Great Barrier Reef and Coral Sea. *Marine and Tropical Sciences Facility (MTSRF) Project*, *2*.

Beck, M. W., Losada, I. J., Menéndez, P., Reguero, B. G., Díaz-Simal, P., & Fernández, F. (2018). The global flood protection savings provided by coral reefs. *Nature Communications*, *9*(1), 2186. https://doi.org/10.1038/s41467-018-04568-z

Bessell-Browne, P., Negri, A. P., Fisher, R., Clode, P. L., Duckworth, A., & Jones, R. (2017). Impacts of turbidity on corals: The relative importance of light limitation and suspended sediments. *Marine Pollution Bulletin*, *117*(1–2), 161–170. https://doi.org/10.1016/j.marpolbul.2017.01.050

Bromirski, P. D., Miller, A. J., Flick, R. E., & Auad, G. (2011). Dynamical suppression of sea level rise along the Pacific coast of North America: Indications for imminent acceleration. *Journal of Geophysical Research: Oceans*, *116*(C7). https://doi.org/10.1029/2010JC006759

Burgess, S. C., Kingsford, M. J., & Black, K. P. (2007). Influence of tidal eddies and wind on the distribution of pre-settlement fishes around One Tree Island, Great Barrier Reef. *Marine Ecology Progress Series*, *341*, 233–242. https://doi.org/10.3354/meps341233

Chazottes, V., Hutchings, P., & Osorno, A. (2017). Impact of an experimental eutrophication on the processes of bioerosion on the reef: One Tree Island, Great Barrier Reef, Australia. *Marine Pollution Bulletin*, *118*(1–2), 125–130. https://doi.org/10.1016/j.marpolbul.2017.02.047

Church, J. A., Hunter, J. R., McInnes, K. L., & White, N. J. (2006). Sea-level rise around the Australian coastline and the changing frequency of extreme sea-level events. *Australian Meteorological Magazine*, *55*(4), 253–260.

Church, J. A., McInnes, K. L., Monselesan, D., & O'Grady, J. (2016). *Sea level rise and allowances for Coastal Councils around Australia - Guidance material (Tech. Rep. No. Report 64)*. CSIRO.

Church, J. A., & White, N. J. (2006). A 20th century acceleration in global sea-level rise. *Geophysical Research Letters*, *33*, 1. https://doi.org/10.1029/2005gl024826

Climate Change Initiative Coastal Sea Level Team. (2020). Coastal sea level anomalies and associated trends from Jason satellite altimetry over 2002-2018. *Scientific Data*, *7*(1), 357. https://doi.org/10.1038/s41597-020-00694-w

Collins, D. S., Avdis, A., Allison, P. A., Johnson, H. D., Hill, J., & Piggott, M. D. (2018). Controls on tidal sedimentation and preservation: Insights from numerical tidal modelling in the Late Oligocene–Miocene South China Sea, Southeast Asia. *Sedimentology*, *65*(7), 2468–2505. https://doi.org/10.1111/sed.12474

Dangendorf, S., Hay, C., Calafat, F. M., Marcos, M., Piecuch, C. G., Berk, K., & Jensen, J. (2019). Persistent acceleration in global sea-level rise since the 1960s. *Nature Climate Change*, *9*(9), 705–710. https://doi.org/10.1038/s41558-019-0531-8

Dangendorf, S., Marcos, M., Woppelmann, G., Conrad, C. P., Frederikse, T., & Riva, R. (2017). Reassessment of 20th century global mean sea level rise. *Proceedings of the National Academy of Sciences*, *114*(23), 5946–5951. https://doi.org/10.1073/pnas.1616007114

Delandmeter, P., Lambrechts, J., Marmorino, G. O., Legat, V., Wolanski, E., Remacle, J. F., et al. (2017). Submesoscale tidal eddies in the wake of coral islands and reefs: Satellite data and numerical modelling. *Ocean Dynamics*, *67*(7), 897–913. https://doi.org/10.1007/s10236-017-1066-z

Devlin, A. T., Jay, D. A., Zaron, E. D., Talke, S. A., Pan, J., & Lin, H. (2017). Tidal variability related to sea level variability in the Pacific Ocean. *Journal of Geophysical Research: Oceans*, *122*, 8445–8463. https://doi.org/10.1002/2017jc013165

Egbert, G. D., & Erofeeva, S. Y. (2002). Efficient inverse modeling of barotropic ocean tides. *Journal of Atmospheric and Oceanic Technology*, *19*(2), 183–204. https://doi.org/10.1175/1520-0426(2002)019<0183:eimobo>2.0.co;2

Gehrels, W. R., Belknap, D. F., Pearce, B. R., & Gong, B. (1995). Modeling the contribution of M2 tidal amplification to the Holocene rise of mean high water in the Gulf of Maine and the Bay of Fundy. *Marine Geology*, *124*(1–4), 71–85. https://doi.org/10.1016/0025-3227(95)00033-u

Geuzaine, C., & Remacle, J. F. (2009). Gmsh: A 3-D finite element mesh generator with built-in pre-and post-processing facilities. *International Journal for Numerical Methods in Engineering*, *79*(11), 1309–1331. https://doi.org/10.1002/nme.2579

Goss, Z., Warder, S., Angeloudis, A., Kramer, S., Avdis, A., & Piggott, M. (2019). Tidal modelling with Thetis: Preliminary English Channel benchmarking.

Green, J. A. M. (2010). Ocean tides and resonance. *Ocean Dynamics*, *60*(5), 1243–1253. https://doi.org/10.1007/s10236-010-0331-1

Greenberg, D. A., Blanchard, W., Smith, B., & Barrow, E. (2012). Climate change, mean sea level and high tides in the Bay of Fundy. *Atmosphere-Ocean*, *50*(3), 261–276. https://doi.org/10.1080/07055900.2012.668670

Hammond, W. C., Blewitt, G., Kreemer, C., & Nerem, R. S. (2021). GPS imaging of global vertical land motion for studies of sea level rise. *Journal of Geophysical Research: Solid Earth*, *126*. https://doi.org/10.1029/2021jb022355

Harker, A., Green, J. A. M., Schindelegger, M., & Wilmes, S.-B. (2019). The impact of sea-level rise on tidal characteristics around Australia. *Ocean Science*, *15*, 1–159. https://doi.org/10.5194/os-15-147-2019

Hill, J. (2019). HRDS: A Python package for hierarchical raster datasets. *Journal of Open Source Software*, *4*(37), 1112. https://doi.org/10.21105/joss.01112

Hoegh-Guldberg, O., Poloczanska, E. S., Skirving, W., & Dove, S. (2017). Coral reef ecosystems under climate change and ocean acidification. *Frontiers in Marine Science*, *4*. https://doi.org/10.3389/fmars.2017.00158

Idier, D., Bertin, X., Thompson, P., & Pickering, M. D. (2019). Interactions between mean sea level, tide, surge, waves and flooding: Mechanisms and contributions to sea-level variations at the coast. *Surveys in Geophysics*, *40*(6), 1603–1630. https://doi.org/10.1007/s10712-019-09549-5

Kärnä, T., De Brye, B., Gourgue, O., Lambrechts, J., Comblen, R., Legat, V., & Deleersnijder, E. (2011). A fully implicit wetting–drying method for DG-FEM shallow water models, with an application to the Scheldt Estuary. *Computer Methods in Applied Mechanics and Engineering*, *200*(5–8), 509–524. https://doi.org/10.1016/j.cma.2010.07.001

Kärnä, T., Kramer, S. C., Mitchell, L., Ham, D. A., Piggott, M. D., & Baptista, A. M. (2018). Thetis coastal ocean model: Discontinuous Galerkin discretization for the three-dimensional hydrostatic equations. *Geoscientific Model Development*, *11*(11), 4359–4382. https://doi.org/10.5194/gmd-11-4359-2018

Kopp, R. E., Kemp, A. C., Bittermann, K., Horton, B. P., Donnelly, J. P., Gehrels, W. R., et al. (2016). Temperature-driven global sea-level variability in the Common Era. *Proceedings of the National Academy of Sciences of the United States of America*, *113*(11), E1434–41. https://doi.org/10.1073/pnas.1517056113

Kramer, S., Kärnä, T., Hill, J., & Funke, S. W. (2020). *stephankramer/uptide*. First release of uptide.

Kuang, C., Liang, H., Mao, X., Karney, B., Gu, J., Huang, H., et al. (2017). Influence of potential future sea-level rise on tides in the China Sea. *Journal of Coastal Research*, *33*(1), 105–117. https://doi.org/10.2112/jcoastres-d-16-00057.1

Lambrechts, J., Comblen, R., Legat, V., Geuzaine, C., & Remacle, J.-F. (2008a). Multiscale mesh generation on the sphere. *Ocean Dynamics*, *58*(5–6), 461–473. https://doi.org/10.1007/s10236-008-0148-3

Lambrechts, J., Hanert, E., Deleersnijder, E., Bernard, P. E., Legat, V., Remacle, J. F., & Wolanski, E. (2008b). A multi-scale model of the hydrodynamics of the whole Great Barrier Reef. *Estuarine, Coastal and Shelf Science*, *79*(1), 143–151. https://doi.org/10.1016/j.ecss.2008.03.016

Ludington, C. (1979). Tidal modifications and associated circulation in a platform reef lagoon. *Australian Journal of Marine & Freshwater Research*, *30*(4), 425–430. https://doi.org/10.1071/MF9790425

Lyard, F., Allain, D., Cancet, M., Carrère, L., & Picot, N. (2020). FES2014 global ocean tides atlas: Design and performances.

McInnes, K. L., Church, J., Monselesan, D., Hunter, J. R., O'Grady, J. G., Haigh, I. D., & Zhang, X. (2015). Information for Australian impact and adaptation planning in response to sea-level rise. *Australian Meteorological and Oceanographic Journal*, *65*(1), 127–149. https://doi.org/10.22499/2.6501.009

Morrison, T., & Hughes, T. (2016). *Climate change and the Great Barrier Reef* (Vol. 1). Policy Information Brief.

National Centers for Environmental Information (NCEI). (2009). ETOPO1 1 Arc-Minute Global Relief Model. https://doi.org/10.7289/V5C8276M

Pelling, H. E., & Green, J. M. (2014). Impact of flood defences and sea-level rise on the European Shelf tidal regime. *Continental Shelf Research*, *85*, 96–105. https://doi.org/10.1016/j.csr.2014.04.011

Pelling, H. E., Green, J. M., & Ward, S. L. (2013). Modelling tides and sea-level rise: To flood or not to flood. *Ocean Modelling*, *63*, 21–29. https://doi.org/10.1016/j.ocemod.2012.12.004

Péquignet, A.-C., Becker, J., Merrifield, M., & Boc, S. (2011). The dissipation of wind wave energy across a fringing reef at ipan, Guam. *Coral Reefs*, *30*(1), 71–82. https://doi.org/10.1007/s00338-011-0719-5

Pickering, M. D., Horsburgh, K. J., Blundell, J. R., Hirschi, J. M., Nicholls, R. J., Verlaan, M., & Wells, N. C. (2017). The impact of future sea-level rise on the global tides. *Continental Shelf Research*, *142*, 50–68. https://doi.org/10.1016/j.csr.2017.02.004

Pickering, M. D., Wells, N. C., Horsburgh, K. J., & Green, J. A. M. (2012). The impact of future sea-level rise on the European Shelf tides. *Continental Shelf Research*, *35*(0), 1–15. https://doi.org/10.1016/j.csr.2011.11.011

Pörtner, H.-O., Roberts, D. C., Masson-Delmotte, V., Zhai, P., Tignor, M., Poloczanska, E., et al. (2019). IPCC special report on the ocean and cryosphere in a changing climate. *IPCC Intergovernmental Panel on Climate Change (IPCC)*.

QGIS.org. (2020). *QGIS Geographic Information System*. Open Source Geospatial Foundation Project.

Rasheed, S., Warder, S. C., Plancherel, Y., & Piggott, M. D. (2020). Response of tidal flow regime and sediment transport in North Male' Atoll, Maldives to coastal modification and sea level rise. *Ocean Sci. Ocean Sci. Discuss*. https://doi.org/10.5194/os-2020-80

RStudio Team. (2020). Rstudio: Integrated development environment for Computer software manual. Retrieved from http://www.rstudio.com/

Seifi, F., Deng, X., & Baltazar Andersen, O. (2019). UoNGBR: A regional assimilation barotropic tidal model for the Great Barrier reef and Coral Sea based on satellite, coastal and marine data. *Remote Sensing*, *11*(19), 2234. https://doi.org/10.3390/rs11192234

Storlazzi, C. D., Elias, E., Field, M. E., & Presto, M. K. (2011). Numerical modeling of the impact of sea-level rise on fringing coral reef hydrodynamics and sediment transport. *Coral Reefs*, *30*(1), 83–96. https://doi.org/10.1007/s00338-011-0723-9

Vouriot, C. V., Angeloudis, A., Kramer, S. C., & Piggott, M. D. (2019). Fate of large-scale vortices in idealized tidal lagoons. *Environmental Fluid Mechanics*, *19*(2), 329–348. https://doi.org/10.1007/s10652-018-9626-4

Wolanski, E., Brinkman, R., Spagnol, S., McAllister, F., Steinberg, C., Skirving, W., & Deleersnijder, E. (2003). Chapter 15 Merging scales in models of water circulation: Perspectives from the great barrier reef. Merging scales in models of water circulation: Perspectives from the great barrier reef. In V. C. Lakhan (Ed.), *Elsevier Oceanography Series. Elsevier*. https://doi.org/10.1016/S0422-9894(03)80132-0

Wolanski, E., & Spagnol, S. (2000). Sticky waters in the Great Barrier reef. Estuarine. *Coastal and Shelf Science*, *50*(1), 27–32. https://doi.org/10.1006/ecss.1999.0528

Woolson, R. F. (2008). Wilcoxon signed-rank test. In *Wiley encyclopedia of clinical trials*. John Wiley & Sons, Ltd. https://doi.org/10.1002/9780471462422.eoct979

World Resources Institute. (2016). Tropical Coral Reefs of the World. Retrieved from https://datasets.wri.org/dataset/tropical-coral-reefs-of-the-world-500-m-resolution-grid

Zhang, X., Church, J. A., Monselesan, D., & McInnes, K. L. (2017). Sea level projections for the Australian region in the 21st century. *Geophysical Research Letters*, *44*(16), 8481–8491. https://doi.org/10.1002/2017GL074176